Global Microbarom Patterns: A First Confirmation of the Theory for Source and Propagation

Marine de Carlo, Patrick Hupe, Alexis Le Pichon, Lars Ceranna, Fabrice Ardhuin

AGU ADVANCING EARTH AND SPACE SCIENCE

Geophysical Research Letters

RESEARCH LETTER
10.1029/2020GL090163

Global Microbarom Patterns: A First Confirmation of the Theory for Source and Propagation

Marine De Carlo[1,2], Patrick Hupe[3], Alexis Le Pichon[1], Lars Ceranna[3], and Fabrice Ardhuin[4]

[1]CEA, DAM, DIF, Arpajon F-91297, France, [2]Université de Bretagne Occidentale, Brest, France, [3]BGR, B4.3, Hannover, Germany, [4]Laboratoire d'Océanographie Physique et Spatiale (LOPS), University of Brest, CNRS, IUEM, Brest, France

Key Points:

- A methodology to predict microbarom arrivals and to compare them with observations is presented
- Performances between two source models accounting for bathymetry, two propagation attenuations, and two wave models are compared
- In more than 90% of the cases, the source model performs better with a radiation depending on the elevation angle than with a monopolar one

Supporting Information:

- Supporting Information S1

Correspondence to:
M. De Carlo,
marine.decarlo@cea.fr

Citation:
De Carlo, M., Hupe, P., Le Pichon, A., Ceranna, L., & Ardhuin, F. (2021). Global microbarom patterns: A first confirmation of the theory for source and propagation. *Geophysical Research Letters*, *48*, e2020GL090163. https://doi.org/10.1029/2020GL090163

Received 1 AUG 2020
Accepted 17 DEC 2020

Abstract Microbarom signals are generated by wind waves at the ocean surface and propagate all around the globe through the stratosphere and ionosphere. Microbaroms dominate the coherent infrasound ambient noise measured worldwide, with a peak around 0.2 Hz. Monitoring these signals allows characterizing the source activity and probing the properties of their propagation medium, the middle atmosphere. Here, we show the first quantitative validation of global microbarom modeling based on ocean wave models, a new source model and atmospheric attenuation. For evaluating these parameters' impact, we compare the modeling results with a global reference database of microbaroms detected by the infrasound International Monitoring System over 7 years. This study demonstrates that the new source model improves the prediction rate of observations by around 20% points against previous models. The performance is enhanced when the new model is combined with a wind-dependent attenuation and an ocean wave model that includes coastal reflection.

Plain Language Summary Microbaroms are atmospheric ambient noise below the human hearing threshold. They are generated by ocean waves and can be detected by infrasound sensors worldwide. A better understanding is important because microbaroms could hide signals of interest in the context of the Comprehensive Nuclear-Test-Ban Treaty, established to unveil clandestine nuclear explosions worldwide. Furthermore, as microbaroms propagate over long ranges through the middle atmosphere, a better knowledge of the received signals provides new insights of middle atmosphere dynamics features that are unresolved in global circulation models. In this study, we use a historical database of microbarom detections to evaluate state-of-the-art models and propose a methodology to simulate microbaroms worldwide.

1. Introduction

Infrasound can propagate over large distances due to low absorption rates and efficient ducting in the stratospheric waveguide. In the 0.05–4-Hz band, infrasound are routinely recorded by the infrasound International Monitoring System (IMS) being deployed to verify compliance with the Comprehensive Nuclear-Test-Ban Treaty (CTBT) (Marty, 2019). As of July 2020, 52 certified stations already provide global coverage of explosive events of both geophysical and anthropogenic origin (Figure 1(a)). These include, for instance, refinery incidents (e.g., Ceranna et al., 2009), natural hazards such as volcanic eruptions (e.g., Matoza et al., 2019), or atmospheric entries of large meteoroids (e.g., Pilger et al., 2019).

Microbarom signals, with frequencies ranging from 0.1 to 0.6 Hz (e.g., Hupe et al., 2019), are dominating the infrasound ambient noise. Originating from ocean surface wave interactions, microbaroms are near-continuously detected worldwide. The detection capability of microbaroms exhibits significant spatiotemporal variation, which is partly controlled by dynamical features of the atmospheric circulation (Ceranna et al., 2019; Landès et al., 2014). Variations in coherent ambient noise result from changes in both the source distribution and the propagation conditions and can be characterized statistically (e.g., Assink et al., 2014). As microbaroms propagate into the middle atmosphere (from around 12 to 90 km altitude), significant features of the vertical structure of the temperature and wind are reflected in the detected signal on the ground. The lack of variability found in both temperature and wind models (e.g., Charlton-Perez et al., 2013; Lee et al., 2019) has motivated the development of atmospheric remote sensing methods for evaluating numerical weather prediction (NWP) model output (e.g., Amezcua et al., 2020; Le Pichon et al., 2015;

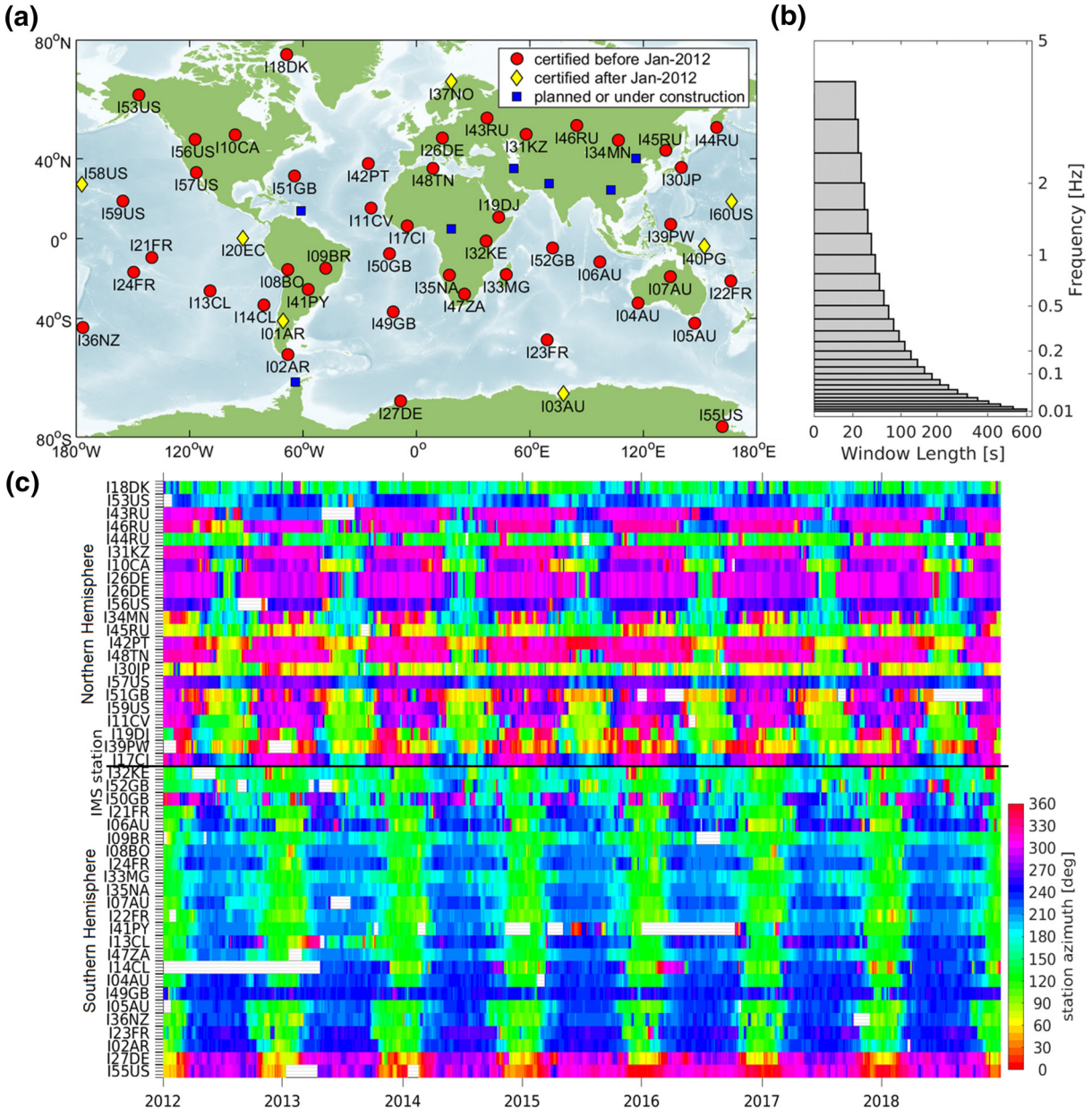

Figure 1. (a) Map of the IMS infrasound network showing the certified and planned stations as of October 2020. Seven of the currently operating stations were not certified before 2012 and are therefore not considered in this study. (b) Third-octave frequency band configuration for the PMCC data processing of the 45 remaining stations. The time step of the processing is 10% of the window lengths (Ceranna et al., 2019). Microbarom detections coincide with log-scaled bands between 0.1 and 0.6 Hz. (c) Global pattern of the microbarom detections during the studied period—each colored line depicts the average back azimuth within (T F02D 7 days, T + 7 days). The time step is 4 days. In the case of missing lines, no microbarom signals were detected within the respective time window, including due to occasionally missing infrasound station data. IMS, International Monitoring System; PMCC, Progressive MultiChannel Correlation.

Vanderbecken et al., 2020). With the increasing number of IMS stations complemented by dense regional networks, systematic studies using historical infrasound data sets and state-of-the-art (re)analysis systems provide useful integrated information on middle atmosphere variability and biases where data coverage is sparse (Blanc et al., 2019). Beyond the atmospheric community, the evaluation of NWP models is essential for the verification of the CTBT, as accurate models are needed to assess the IMS network performance in higher resolution and reduce source location errors.

Improving the source knowledge of microbaroms is critical for operational infrasound monitoring as coherent noise may interfere with the detection and identification of transient signals being emitted by events of

interest. Various microbarom energy spectrum models have been developed in earlier works. Brekhovskikh et al. (1973) and Ardhuin and Herbers (2013) considered an infinite depth ocean with the radiative pressure depending on the wave elevation angle. Waxler and Gilbert (2006) and Waxler et al. (2007) investigated infrasound radiated by ocean waves in finite depth ocean from monopolar sources. More recently, De Carlo et al. (2020) developed a source model accounting for both directivity and water depth effects allowing to better characterizing the source of microbaroms.

In this study, a multiyear and global reference database of microbaroms recorded by the IMS network is constructed using logarithmically scaled frequency bands between 0.01 and 4 Hz. Systematic comparisons between the modeled and observed directional amplitudes of microbaroms over 7 years provide new insights on coupling mechanisms at the ocean–atmosphere interface and long-range propagation effects. Data and methods are presented in Section 2. The main results are given in Section 3. Discussion and conclusions follow in Sections 4 and 5.

2. Data and Methods

2.1. IMS Observations

The CTBT Organisation Preparatory Commission certified 45 of the IMS infrasound stations before 2012 (Figure 1(a)); hence covering the whole studied period (from 2012 to 2018). IMS infrasound array data are routinely processed at the International Data Center (Mialle et al., 2019) using the Progressive MultiChannel Correlation (PMCC) method (Cansi, 1995). The PMCC algorithm automatically processes continuous waveforms in successive, overlapping time windows and adjacent frequency bands to detect coherent plane waves within the background noise. Each detected arrival is characterized by wavefront parameters—for example, back azimuth, frequency, and root-mean-square amplitude—derived from the time delays between pairs of sensor triplets. Distant sensors within an array are progressively added during the processing to enhance the quality of the detected parameters (e.g., Ceranna et al., 2019). Adjacent detections in individual time–frequency cells exhibiting similar wavefront parameters are clustered into a family.

A practical benefit was gained by implementing PMCC with a variable window length and log-spaced frequency bands, allowing the efficient process of the full frequency range in a single computational run (e.g., Brachet et al., 2010). With this implementation, a first global and multiyear systematic broadband (0.01–5 Hz) analysis of historical IMS records was performed by Matoza et al. (2013). The PMCC configuration has been refined for reprocessing the IMS infrasound data set; it relies on 27 third-octave frequency bands between 0.01 and 4 Hz, with window lengths varying from 600 s down to 30 s, respectively (Figure 1(b)). This configuration allows computationally efficient broadband processing and accurate estimates of frequency-dependent wave parameters useful for source separation (Ceranna et al., 2019). A detection is considered as a microbarom signal if its center frequency covers the 0.1–0.6 Hz interval and if, for reasons of significance, the family size is larger than 40, because events with more arrival pixels are generally of larger amplitudes or, for instance, longer durations.

Figure 1(c) summarizes the microbarom detections at 45 IMS stations from 2012 to 2018. In the Northern Hemisphere (NH), the majority of the signals originate from North Pacific, Atlantic, and Indian Oceans. In the Southern Hemisphere (SH), signals essentially originate from large swell systems circulating along the Antarctic Circumpolar Current (ACC). The seasonal oscillation of the dominant azimuths correlates with the seasonal reversal of the stratospheric wind (e.g., Landès et al., 2014), especially at the midlatitudes where the strongest winds in both the troposphere and the stratosphere drive the sources and the propagation, respectively. Notable outliers from the seasonal pattern in the NH are I30JP, I44RU, and I45RU, caused by the lack of strong sources to the west of these stations (see Figure 1(a)). In the SH, I49GB exhibits hardly varying westerly back azimuths. I49GB is located at the western bottom of the volcano island Tristan da Cunha; hence, despite being surrounded by potential microbarom sources, arrivals from easterly directions are shadowed by the steep volcano flank.

2.2. Source and Propagation Modeling

Ocean waves are generally well represented by a sum of many sine waves with random phases. Their local statistical properties are given by the power spectral density of the surface elevation , also called

the "wave spectrum," which gives the distribution of the surface elevation variance as a function of wave frequency f and azimuth of ocean wave propagation θ. Ocean wave models such as WAVEWATCHIII® (WAVEWATCH III Development Group (WW3DG), 2016) provide an estimate of $E(f,\theta)$ and its evolution in space and time, based on the surface wind fields. Such models account for wave generation by the wind, propagation (including slow nonlinear evolution), and dissipation dominated by wave breaking. For the application to microseisms and microbaroms, the magnitude of wave energy in opposite directions is particularly important, because microbaroms are generated by second-order nonlinear interactions of almost opposing ocean waves. The source at the acoustic frequency f_s is proportional to $H(f_s)$, the Hasselmann integral (Hasselmann, 1963),

$$H(f_s) = \int_0^{2\pi} E\left(\frac{f_s}{2},\theta\right) \cdot E\left(\frac{f_s}{2},\theta+\pi\right) d\theta \tag{1}$$

The Hasselmann integral is obtained from the *p2l* output of the numerical wave model (WW3DG, 2016) at a 3-h temporal and a 0.5° × 0.5° spatial resolution, corresponding to the modeled second-order equivalent surface pressure due to ocean wave interaction:

$$p2l\left(\frac{f_s}{2}\right) = \frac{1}{2}\rho_w^2 g^2 H(f_s) \tag{2}$$

where ρ_w is the density of water and g is the gravity acceleration. Following the developments of Waxler et al. (2007) and De Carlo et al. (2020), sources radiating in azimuth φ can be expressed in terms of pressure spectrum F_{p2} and correspond to a sum over all elevation angles θ_a:

$$F_{p2}(\varphi, f_s) = \frac{2\,\rho_a^2\, g^2\, \pi^2 f_s^3}{c_a^2} H(f_s) \int_{\theta_a=0}^{\pi/2} |R_a|^2 \cos\theta_a \sin\theta_a d\theta_a \tag{3}$$

where ρ_a and c_a are the air density and the speed of sound in the air, respectively. R_a is a coefficient accounting for finite depth ocean depending on the source model chosen (De Carlo et al., 2020).

In this study, two models are confronted: (i) a monopolar source—that is, no dependency on the elevation angle for R_a and thus a high bathymetry impact—as proposed by Waxler et al. (2007), hereinafter referred to as W07, and (ii) a nonmonopolar source with R_a depending on the elevation angle (De Carlo et al., 2020), hereinafter DC20. A major source of model uncertainty is the reflection of ocean waves off the coast (Ardhuin et al., 2013). For this reason, two parameterizations of coastal reflection are used: (i) one without reflection ("NO REF") and (ii) the other one with reflection coefficients of 10% on the continents, 20% on the islands, and 40% on the ice ("REF102040").

As the main objective of this study is to run massive simulations (45 stations over 7 years) using different models and to compare these outputs with PMCC processing results, propagation simulation with low calculation effort is needed. A dedicated, 2D or 3D infrasound propagation model such as provided by the NCPAprop package (Waxler et al., 2017) would be capable of accurate long-range simulations. However, for this study, these simulations would require a huge computational effort, which may amount to around 30 h per station and time step (depending on the Information Technology (IT) infrastructure). A generalized attenuation law, such as the semiempirical one proposed by Le Pichon et al. (2012, their Equation 2), lowers the accuracy in terms of transmission loss but requires much less computation time; here, the computation takes less than 30 min per station and per year (using a comparable IT infrastructure). This attenuation relation provides the pressure attenuation $Att(f_s)$, which accounts for the propagation range, the source frequency f_s, and the stratospheric effective sound speed ratio $V_{eff-ratio}(\varphi)$ (ratio between the effective sound speed at 50 km altitude and the sound speed at the ground level in the direction of propagation φ). Tailpied (2016) showed that the uncertainty associated with this law—accounting for both numerical and wind uncertainties of 5%—lays within 10 dB for frequencies under 0.4 Hz and sources beyond the shadow zone (around 200 km). Such an uncertainty makes the comparison of different models using the distance between modeled and observed amplitudes irrelevant. In order to overcome this issue, this study considers the normalized directional acoustic spectra, and remaining uncertainty effects are washed out both by the monthly averaging of the metric defined in Section 2.3 and by the use of the global database.

The attenuation relative to the considered station is computed for each cell of the source model. Then, the source pressure spectrum $F_{p2}(\varphi, f_s)$ is multiplied by the square of the attenuation Att and by the cell area dS_i. To compute the directional acoustic spectrum $F_{p2-sta}(\varphi, f_s)$ at the station, cells (i) intersecting azimuthal bands of 1° resolution are summed:

$$F_{p2-sta}(\varphi, f_s) = \sum_{\substack{i|\varphi_i=\varphi \\ i|r_i \leq 5{,}000\,\mathrm{km}}} F_{p2}(\varphi_i, f_s) \times Att_i(f_s)^2 \times dS_i \quad (4)$$

We constrain the summation to cells of maximum distances of 5,000 km from the station. The attenuation law was defined for ranges up to 3,000 km; however, dominant sources tend to be further away from the stations. Therefore, we extrapolate the law as it has already been done successfully for single station studies (e.g., Hupe et al., 2019).

Another simplification concerns the parameterization of the propagation conditions, which naturally vary along the propagation path. We account for 1D temperature and wind profiles at the station for calculating the $V_{eff-ratio}$, introducing the well-known directivity in the propagation depending on the vertical structure of the wind field. These profiles are obtained from the operational high-resolution analysis produced by the Integrated Forecast System of the European Centre for Medium-Range Weather Forecasts (ECMWF, HRES IFS cycle 38r2, http://www.ecmwf.int). We compute a second parameterization representing isotropic propagation conditions (windless atmosphere, i.e., $V_{eff-ratio} = 1$). This serves for validation purposes of the methodology as the source models should perform better with the more realistic wind parameterization.

2.3. Observations and Model Comparisons

For each modeling configuration, the output consists of an acoustic directional spectrum with 1° resolution in direction and frequency bands of 0.1 Hz width for each model time step of 3 h. The observation database, however, consists of detections unevenly distributed in time, from a few detections to hundreds of detections within 3 h, and thus varying wavefront parameters are obtained. The direction of origin of the incoming wavefront is calculated at IMS stations with an uncertainty of few degrees (Szuberla & Olson, 2004) and the standard deviation of the origin directions within 3 h varies widely, with an average deviation of 15°. Therefore, a quantitative comparison between the observations and the model needs to account for all sources and their spatial dimension.

For each time step and frequency band, the directional distribution of the modeled signals (Equation 4) is normalized by its maximum over all azimuths, as shown in Figure 2(a), in order to overcome uncertainty issues arising from the attenuation law considered. Then, a threshold is applied to the normalized distribution, below which the predicted signals are discarded. All detections are classified into predicted and non-predicted observations (Figure 2(b)), according to their arrival time, azimuth (1° resolution), and frequency. This allows the definition of a proxy to evaluate the models: the coefficient of predicted observation (CPO) is the ratio of predicted observations to all observations. Setting the threshold to 0.4 is an optimal trade-off between the CPO and the false-positive rate (Supporting Information S1, Figure S3).

The modeled pressure spectrum relies on three parameters: (i) coastal reflection effects in wave modeling—"No REF" or "REF102040," (ii) stratospheric propagation effects, taken as a methodology reference—$V_{eff-ratio}(\varphi)$ equal to 1 ("NoWind") or taken at the station ("WindSta"), and (iii) the source model—W07 or DC20. Consequently, eight parameterizations are run, and for each of them, the CPO is computed for each station, frequency band, and month over the 7 years.

3. Results

Overall, we obtained 151,200 CPO values. For each modeling parameter, the CPO values compare as follows: DC20 (respectively WindSta and REF102040) results in higher CPO values than W07 (resp. NoWind and NOREF) in 90% of the cases (resp. 68% and 60%).

Figure 3 shows the CPO variations along the IMS stations (3a), the months (3b and 3d), frequency bands (3c), and the years (3e) for the eight simulations. Two main results are noted. First, for all those parameters,

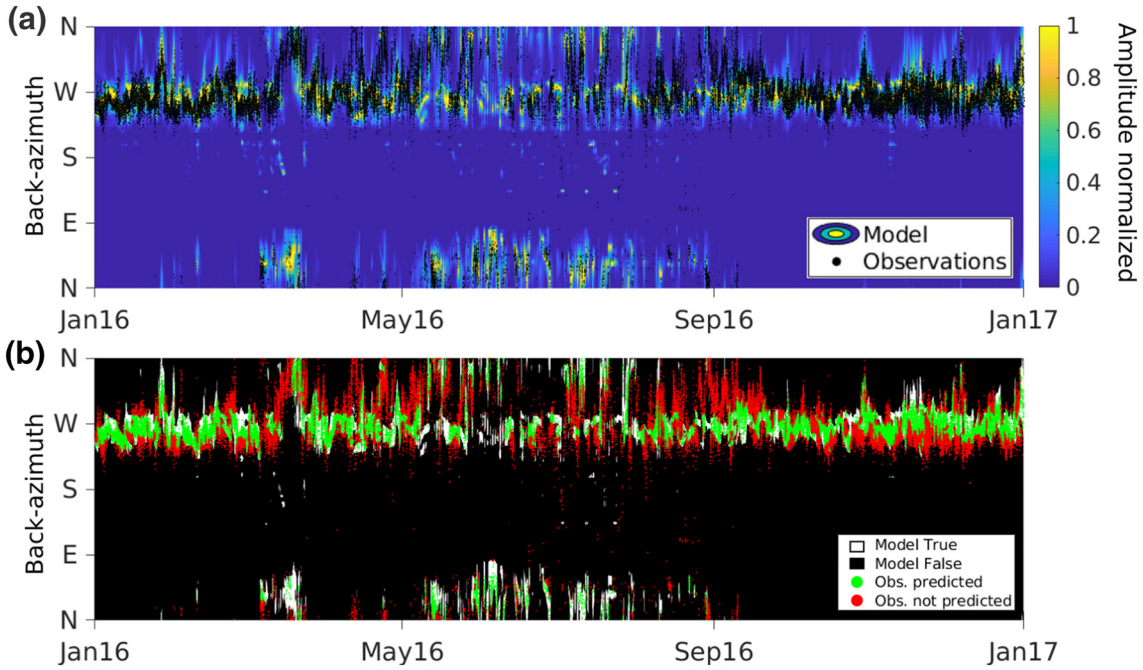

Figure 2. Comparison methodology between model—with the configuration DC20, WindSta, REF102040—and detections shown for I37NO, Norway for [0.2–0.3] Hz. (a) Azimuth distribution of the modeled amplitude (normalized per time step). All detections are depicted by black dots. (b) After the application of a threshold to the normalized amplitude—here 0.4—the detections are classified into predicted (green) and unpredicted (red) detections. Modeled directions of microbarom arrivals are highlighted in white, whereas black depicts unfavorable directions according to the model.

the configuration with REF102040, WindSta, and DC20 has clearly the highest CPO value in the majority of cases with the second best configuration being mostly the one with NOREF, WindSta, and DC20. Second, in almost all cases, there is a CPO difference of roughly 0.15 between the configurations with the DC20 and those with the W07 source model.

Figure 3(a) illustrates the CPO variations along the IMS stations, ordered by latitude. The configuration combining DC20, coastal reflection, and wind at the station yields a CPO that varies between 0.15 at I34MN and 0.8 at I05AU and is the configuration with the highest CPO value for all but six stations (13.3%) where it is topped by the same configuration with NoWind. For 34 of 45 stations, more than half of the observations are predicted using this configuration (CPO $\geq$ 0.5), and for eight of these stations, the CPO exceeds 0.7. In contrast, the lowest CPO values—generally obtained with W07, isotropic propagation conditions, and no coastal reflection—range from 0.07 at I34MN to 0.47 at I44RU.

The monthly variation of the CPO differs with the hemisphere. In the NH (Figure 3(b)), the pattern is similar for the eight configurations, whereas in the SH (Figure 3(d)), the pattern mainly depends on whether the wind is accounted for or not. In the NH, for each configuration, the CPO decreases by less than 0.1 during the summer months and is mostly stable during other months. This decrease could be related to more scattered sources in the summer, whereas major sources occur during the winter and are mostly located upwind, west of the stations, which coincides with the prevailing wind direction. One may note that configurations with WindSta are better than their counterparts by between 0.025 and 0.05 CPO points, except in April, May, and September, when both parameterizations yield quite similar CPO values. These months correspond to weaker zonal winds around the stratospheric wind reversal periods, hence the WindSta and NoWind parameterizations converge. This effect is also evident in the SH in March, October, and November. The annual CPO minima in these months, in which $V_{eff-ratio}$ is close to one, may be caused by gravity waves perturbing the unstable waveguide conditions while not being resolved in ECMWF models (Hupe et al., 2019).

In the SH, configurations with NoWind are almost constant over the months presenting only a slight increase in March, October, and November (maximum CPO = 0.54). On the contrary, WindSta configurations

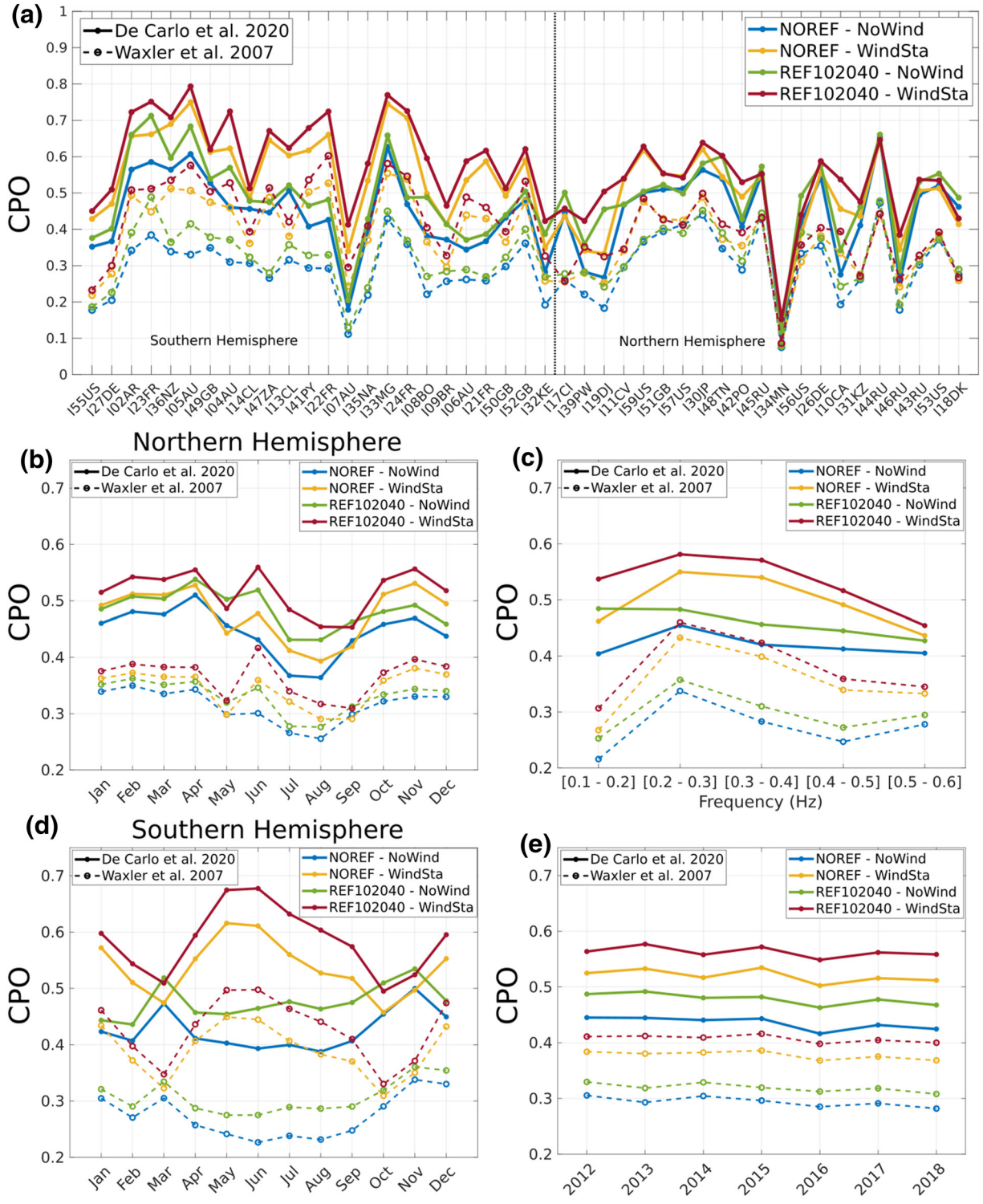

Figure 3. CPO variations against output parameters—stations (ordered by latitude), months, years, and frequency—for the eight modeling configurations. Solid lines represent configurations with the DC20 source model, while dashed lines correspond to configurations with the W07 source model. Configurations with parameters NOREF–NoWind, NOREF–WindSta, REF102040–NoWind, and REF102040–WindSta are respectively colored in blue, yellow, green, and red. (a) Variations over the 45 IMS stations. (b) Monthly variations for stations in the Northern Hemisphere. (c) Variations over the frequency bands. (d) Monthly variations for stations in the Southern Hemisphere. (e) Variations over the 7 years of this study. CPO, coefficient of predicted observation; IMS, International Monitoring System.

show seasonal amplitude variations of the CPO of more than 0.1 CPO points, with a maximum during austral winter in June (0.68), a secondary maximum during summer in December (0.6), and the aforementioned minima in March and October (0.5). These variations correspond to the presence of strong sources the whole year in the SH, as fewer landmasses allow microbarom sources to exist throughout the whole ACC. Therefore, the stratospheric wind parameterization is the key to detecting and predicting the actual sources of microbaroms as it controls the propagation direction.

Figure 3(c), representing the CPO variations with the frequency, shows the highest CPO values for the frequency bands [0.2–0.3] Hz and [0.3–0.4] Hz. For the configurations with the source model W07, the lowest CPO values (0.21–0.31) are obtained for the lowest frequency band ([0.1–0.2] Hz) whereas for configurations with DC20, the highest frequency band ([0.5–0.6] Hz) shows the lowest CPO values (0.40–0.46). Configurations with WindSta yield higher CPO values than their counterparts with NoWind, with a CPO difference varying from 0.025 to 0.1 CPO points, and the largest differences result for the mid frequencies [0.2–0.5] Hz. One may note that for [0.1–0.2] Hz, with the DC20 source model, coastal reflection shows some impact as both configurations with REF102040 have higher CPO values than both configurations with NOREF.

Figure 3(e) shows almost constant CPO values along the years for each configurations, and there is likely no yearly variation.

4. Discussion

The DC20 source model by De Carlo et al. (2020) improves the microbarom predictions against the previously established W07 model by Waxler et al. (2007) such that the CPO increases by 0.15 CPO points. The modeling results concerning the wind parameterization suggest that the general approach is justified, as the WindSta parameterization mostly results in higher CPO scores than NoWind configurations for both source models. In this context, the exceptions around the equinoxes, when the $V_{eff-ratio}$ is closer to one, support this argumentation and highlight the importance of enhancing atmospheric models toward well-resolved small-scale fluctuations.

Apart from more realistic but computation-expensive 3D propagation modeling as a different approach, a more sophisticated parameterization of the propagation conditions would also be desirable. The use of 1D profiles for determining the $V_{eff-ratio}$ is not just a simplification of the propagation conditions but also poses the question of the profile choice. Here, we focused on atmospheric conditions at the IMS stations because these are crucial for detecting a signal. Moreover, this approach is computationally more cost efficient than considering the $V_{eff-ratio}$ at the source—that is, each grid point of the model—or even averaging along the propagation paths. For mainly zonal propagation paths, the conditions will not differ too much, and samples conducted for this study relying on the source profiles have indicated only marginal differences in CPO scores. However, further studies are required to investigate this effect for the equinox periods as well as for outlier stations.

The ability to predict detections at outlier stations, such as I34MN (CPO < 0.2), is significantly limited for all parameterizations. This station in Mongolia is far from any major microbarom sources, especially the Northern Atlantic hotspot (>6,000 km), which coincides with the preferred arrival direction in the NH (Figure S2 in the Supporting Information). For this station, the parameterized propagation, constrained to 5,000 km, excludes sources that would contribute the most to the detections. Furthermore, during summertime, the station does not receive any signal competing with the major sources from the SH; therefore, the assumption of uniform atmosphere along the propagation is no longer valid here. These constraints are also applicable to I46RU (CPO between 0.18 and 0.39) and I31KZ to a lesser extent (CPO between 0.26 and 0.48).

Unlike for microseism simulations where the coastal reflection is of great importance, the impact of coastal reflection for microbaroms is almost negligible. This is likely explained by a higher sensibility to atmospheric propagation effects on microbaroms, thus limiting the impact of the wave model's coastal parameterizations.

The metric was chosen to favor a model with more predicted observations. However, the false-positive rate—false positive corresponds to predicted arrivals without any observation—can also be of importance.

Of specific interest is the increase of the false-positive rate in windless propagation (21% vs. 11% in a windy atmosphere), as this underlines the well-known importance of accounting for realistic wind in the propagation and thus additionally validates our general modeling approach. Overall, in order to limit the false-positive impact, the threshold for the model binarization was set to 0.4. A smaller threshold would have increased CPO values along with the false-positive rate—for example, for a threshold of 0.1 (respectively 0.4), the mean CPO value is 0.77 (0.43) and the mean false-positive rate is 38% (14%).

Another limitation of this study lies in the known drawbacks of the conventional detection algorithm to characterize the interfering microbarom wavefields originating from different sources. The use of high-resolution detection processing techniques capable of extracting multidirectional coherent energy could contribute to an enhanced assessment of the model prediction capability at stations where secondary sources compete with the major ones (e.g., Den Ouden et al., 2020).

5. Conclusions

This study, supported by the reprocessed archive of continuous IMS waveform data, shows that modeling microbaroms worldwide in a straightforward way is feasible and yields overall satisfactory results. The introduced metric allows assessing the different model parameters quantitatively. The analysis for 45 infrasound stations leads to the conclusion that the source model recently developed by De Carlo et al. (2020) enables higher prediction rates than the previously established source model. Modeling microbarom signals worldwide is further enhanced by combining the new source model, numerical wave model with coastal reflection enabled, and propagation accounting for the stratospheric wind at the station.

Further studies should consider propagation over very large distances—more than 5,000 km—and atmospheric variations along the propagation paths to enhance the simulations, especially for outlier stations. Also, additional studies are required to explore time-dependent and range-dependent full-wave propagation techniques (e.g., Waxler & Assink, 2019), while still maintaining computational efficiency. Applying such approaches would allow accounting for globally distributed microbarom sources.

Acknowledgments
This work was supported by the ISblue project, Interdisciplinary graduate school for the blue planet (ANR-17-EURE-0015) and cofunded by a grant from the French government under the program "Investissements d'Avenir." The infrasound data have been processed using the PMCC software v5.7.4, developed at CEA (Département Analyse, Surveillance, Environnement). Access to the IMS network's data including differential pressure recordings of the infrasound stations is available to National Data Centers of the CTBTO and can be made available to others upon request through the virtual Data Exploitation Center (vDEC) at https://www.ctbto.org/specials/vdec (last accessed on July 21, 2020). The operational high-resolution atmospheric model analysis, produced by the Integrated Forecast System of the ECMWF, is accessible via https://www.ecmwf.int/en/forecasts/datasets (last accessed on July 21, 2020). The modeled second-order equivalent surface pressure due to ocean wave interaction is calculated by IFREMER and, at this time, is only available at ftp://ftp.ifremer.fr/ifremer/ww3/HINDCAST/SISMO (last accessed on July 21, 2020).

References

Amezcua, J., Näsholm, S. P., Blixt, E. M., & Charlton-Perez, A. J. (2020). Assimilation of atmospheric infrasound data to constrain tropospheric and stratospheric winds. *Quarterly Journal of the Royal Meteorological Society*, *146*, 2634–2653. https://doi.org/10.1002/qj.3809

Ardhuin, F., & Herbers, T. H. C. (2013). Noise generation in the solid Earth, oceans and atmosphere, from nonlinear interacting surface gravity waves in finite depth. *Journal of Fluid Mechanics*, *716*, 316–348.

Ardhuin, F., Lavanant, T., & Obrebski, M. (2013). A numerical model for ocean ultra-low frequency noise: Wave-generated acoustic-gravity and Rayleigh modes. *Journal of the Acoustical Society of America*, *134*(4), 3242–3259.

Assink, J., Waxler, R., Smets, P., & Evers, L. (2014). Bidirectional infrasonic ducts associated with sudden stratospheric warming events. *Journal of Geophysical Research: Atmospheres*, *119*, 1140–1153. https://doi.org/10.1002/2013JD021062

Blanc, E., Pol, K., Le Pichon, A., Hauchecorne, A., Keckhut, P., Baumgarten, G., et al. (2019). Middle atmosphere variability and model uncertainties as investigated in the framework of the ARISE project. In *Infrasound monitoring for atmospheric studies* (2nd ed., pp. 845–887). Dordrecht: Springer.

Brachet, N., Brown, D., Le Bras, R., Cansi, Y., Mialle, P., & Coyne, J. (2010). Monitoring the Earth's atmosphere with the global IMS infrasound network. In *Infrasound monitoring for atmospheric studies* (pp. 77–118). Dordrecht: Springer.

Brekhovskikh, L. M., Goncharov, V. V., Kurtepov, V. M., & Naugolnykh, K. A. (1973). The radiation of infrasound into the atmosphere by surface-waves in the ocean. *Izvestiya Akademii Nauk SSSR Fizika Atmosfery i Okeana*, *9*(9), 899–907.

Cansi, Y. (1995). An automatic seismic event processing for detection and location: The PMCC method. *Geophysical Research Letters*, *22*(9), 1021–1024.

Ceranna, L., Le Pichon, A., Green, D., & Mialle, P. (2009). The Buncefield explosion: A benchmark for infrasound analysis across Central Europe. *Geophysical Journal International*, *177*(2), 491–508.

Ceranna, L., Matoza, R., Hupe, P., Le Pichon, A., & Landès, M. (2019). Systematic array processing of a decade of global IMS infrasound data. In *Infrasound monitoring for atmospheric studies* (2nd ed., pp. 471–482). Dordrecht: Springer.

Charlton-Perez, A. J., Baldwin, M. P., Birner, T., Black, R. X., Butler, A. H., Calvo, N., et al. (2013). On the lack of stratospheric dynamical variability in low-top versions of the CMIP5 models. *Journal of Geophysical Research: Atmospheres*, *118*, 2494–2505. https://doi.org/10.1002/jgrd.50125

De Carlo, M., Ardhuin, F., & Le Pichon, A. (2020). Atmospheric infrasound radiation by ocean waves in finite depth: Unified generation theory and application to radiation patterns. *Geophysical Journal International*, *221*(1), 569–585.

Den Ouden, O. F., Assink, J. D., Smets, P. S., Shani-Kadmiel, S., Averbuch, G., & Evers, L. G. (2020). CLEAN beamforming for the enhanced detection of multiple infrasonic sources. *Geophysical Journal International*, *221*(1), 305–317.

Hasselmann, K. (1963). A statistical analysis of the generation of microseisms. *Reviews of Geophysics*, *2*(1), 177–210.

Hupe, P., Ceranna, L., Pilger, C., De Carlo, M., Le Pichon, A., Kaifler, B., & Rapp, M. (2019). Assessing middle atmosphere weather models using infrasound detections from microbaroms. *Geophysical Journal International*, *216*(3), 1761–1767.

Landès, M., Le Pichon, A., Shapiro, N. M., Hillers, G., & Campillo, M. (2014). Explaining global patterns of microbarom observations with wave action models. *Geophysical Journal International*, *199*(3), 1328–1337.

Lee, C., Smets, P., Charlton-Perez, A., Evers, L., Harrison, G., & Marlton, G. (2019). The potential impact of upper stratospheric measurements on sub-seasonal forecasts in the extra-tropics. In *Infrasound monitoring for atmospheric studies* (2nd ed., pp. 889–907). Dordrecht: Springer

Le Pichon, A., Assink, J., Heinrich, P., Blanc, E., Charlton-Perez, A., Lee, C. F., et al. (2015). Comparison of co-located independent ground-based middle atmospheric wind and temperature measurements with numerical weather prediction models. *Journal of Geophysical Research: Atmospheres*, *120*, 8318–8331. https://doi.org/10.1002/2015JD023273

Le Pichon, A., Ceranna, L., & Vergoz, J. (2012). Incorporating numerical modeling into estimates of the detection capability of the IMS infrasound network. *Journal of Geophysical Research*, *117*, D05121. https://doi.org/10.1029/2011JD016670

Marty, J. (2019). The IMS infrasound network: Current status and technological developments. In *Infrasound monitoring for atmospheric studies* (2nd ed., pp. 3–62). Dordrecht: Springer.

Matoza, R. S., Fee, D., Green, D., & Mialle, P. (2019). Volcano infrasound and the International Monitoring System. In *Infrasound monitoring for atmospheric studies* (2nd ed., pp. 1023–1077). Dordrecht: Springer.

Matoza, R. S., Landès, M., Le Pichon, A., Ceranna, L., & Brown, D. (2013). Coherent ambient infrasound recorded by the International Monitoring System. *Geophysical Research Letters*, *40*, 429–433. https://doi.org/10.1029/2012GL054329

Mialle, P., Brown, D., & Arora, N., Colleagues from IDC. (2019). Advances in operational processing at the International Data Centre. In *Infrasound monitoring for atmospheric studies* (2nd ed., pp. 209–248). Dordrecht: Springer.

Pilger, C., Ceranna, L., Le Pichon, A., & Brown, P. (2019). Large meteoroids as global infrasound reference events. In *Infrasound monitoring for atmospheric studies* (2nd ed., pp. 451–470). Dordrecht: Springer.

Szuberla, C. A., & Olson, J. V. (2004). Uncertainties associated with parameter estimation in atmospheric infrasound arrays. *Journal of the Acoustical Society of America*, *115*(1), 253–258.

Tailpied, D. (2016). *Évaluation et optimization de réseau infrason pour la surveillance volcanique* (PhD thesis) [in French]. France: Institut de Physique du Globe de Paris.

Vanderbecken, P., Mahfouf, J.-F., & Millet, C. (2020). Bayesian selection of atmospheric profiles from an ensemble data assimilation system using infrasonic observations of May 2016 Mount Etna Eruptions. *Journal of Geophysical Research: Atmospheres*, *125*, e2019JD031168. https://doi.org/10.1029/2019JD031168

WAVEWATCH III Development Group (WW3DG). (2016). User manual and system documentation of WAVEWATCH III version 5.16. *NOAA/NWS/NCEP/MMAB Technical Note 329*, 1–326.

Waxler, R., & Assink, J. (2019). Propagation modeling through realistic atmosphere and benchmarking. In *Infrasound monitoring for atmospheric studies* (2nd ed., pp. 509–549). Dordrecht: Springer.

Waxler, R., Assink, J., Hetzer, C., & Velea, D. (2017). NCPAprop—A software package for infrasound propagation modeling. *Journal of the Acoustical Society of America*, *141*, 3627. https://doi.org/10.1121/1.4987797

Waxler, R., & Gilbert, K. (2006). The radiation of atmospheric microbaroms by ocean waves. *Journal of the Acoustical Society of America*, *119*(5), 2651–2664.

Waxler, R., Gilbert, K., Talmadge, C., & Hetzer, C. (2007). The effect of the finite depth of the ocean on microbarom signals. *Paper presented at 8th International Conference on Theoretical and Computational Acoustics (ICTCA)*. Crete, Greece.